High-fidelity Optimal Control Laws to Characterize the Maneuvering Capabilities of Earth-bound Solar Sails

Carzana, L.; Visser, P.N.A.M.; Heiligers, M.J.

Publication date
2024

Document Version
Final published version

Published in
Proceedings of the 75th International Astronautical Congress 2024

75th International Astronautical Congress (IAC), Milan, Italy, 14-18 October 2024.

IAC–24–C.1.2.4

High-fidelity Optimal Control Laws to Characterize the Maneuvering Capabilities of Earth-bound Solar Sails

Livio Carzana[a*], Pieter Visser[b], Jeannette Heiligers[c]

[a] *Faculty of Aerospace Engineering, Delft University of Technology, Kluyverweg 1, 2629 HS Delft, L.Carzana@tudelft.nl*
[b] *Faculty of Aerospace Engineering, Delft University of Technology, Kluyverweg 1, 2629 HS Delft, P.N.A.M.Visser@tudelft.nl*
[c] *Faculty of Aerospace Engineering, Delft University of Technology, Kluyverweg 1, 2629 HS Delft, M.J.Heiligers@tudelft.nl*
[*] *Corresponding author*

Abstract

Solar sailing is a propulsion method that uses solar radiation pressure (SRP) as main source of thrust and is therefore particularly suited for heliocentric flight regimes. However, the vast majority of sailcraft launched to date have flown around Earth, as will those scheduled for launch in the near future. Around the Earth, the dynamics of a solar sail are affected by the presence of eclipses and additional sources of acceleration apart from SRP, in particular, atmospheric drag and the Earth's planetary radiation pressure (PRP). These accelerations can reach magnitudes in the order of (or even larger than) the SRP acceleration and, therefore, they can potentially be exploited to manoeuvre more effectively around the Earth. Nevertheless, the majority of research conducted on Earth-bound solar sailing either neglects these accelerations or treats them as uncontrollable sources of perturbation. In light of this, this paper presents a high-fidelity trajectory optimisation method which is then used to thoroughly characterise the manoeuvring capabilities of solar sails in the near-Earth environment. The optimisation algorithm is designed to change any orbital element in a locally optimal manner while accounting for the SRP, PRP, aerodynamic, and gravitational accelerations. To tune the optimiser, a first-order analysis of the accelerations achievable by sailcraft in proximity of the Earth is discussed. Then, the optimisation algorithm is exploited to fully characterise the manoeuvring capabilities of Earth-bound solar sails, taking NASA's recently-launched ACS3 solar-sail mission as a baseline. Specifically, different parametric analyses are conducted to determine ACS3's orbit-raising and inclination-changing capabilities for a large set of orbits, solar activities, and sailcraft characteristics. The results of this study not only enhance the understanding of ACS3's performance but also provide valuable insights for the mission design of future Earth-bound solar-sail missions for a variety of mission applications, such as active-debris removal and in-orbit servicing.

Keywords: solar sail, mission design, manoeuvring capabilities, planetary radiation pressure, orbit raising, inclination change

Acronyms/Abbreviations

ACS3 Advanced Composite Solar Sail System
AE acceleration envelope
ARP albedo radiation pressure
BBRP blackbody radiation pressure
LTAN local time of the ascending node
PRP planetary radiation pressure
SRP solar radiation pressure

1. Introduction

Solar sailing is a propulsion method that takes advantage of solar radiation pressure (SRP) as primary source of thrust [1]. Therefore, unlike traditional propulsion systems, solar sails can deliver continuous thrust without relying on fuel, making them a potentially viable option for long-duration mission applications. The interest that solar sailing has drawn over the last decades has resulted in several studies investigating its use for a variety of Earth-bound and interplanetary missions [2–4]. It has also led to the development and launch of the first solar-sail technology demonstration missions, which have predominantly remained around Earth. Among these is NASA's Advanced Composite Solar Sail System (ACS3) mission, launched in April 2024 to demonstrate the in-orbit deployment and manoeuvring capabilities of NASA's latest solar-sail technology [5]. Like ACS3, the majority of future solar-sail missions are expected to be launched into Earth-orbit, with the objective to assess or exploit the potential of solar sailing for different Earth-bound mission applications [6]. To do so effectively, however, accurate knowledge of the near-Earth dynamical environment and how this environment affects the sailcraft controllability is required. This task is rendered particularly challenging by the complex solar-sail dynamics in proximity of the Earth, which are characterised by the pres-

ence of eclipses, gravitational perturbations, and the accelerations due to atmospheric drag and planetary radiation pressure (PRP). These accelerations can achieve magnitudes in the order of – or even larger than – the SRP acceleration [7]. Therefore, taking them into account in the dynamics and sailcraft control is essential to accurately predict the sailcraft's manoeuvring capabilities. Despite this need, research exploring how to effectively leverage the different contributions to the solar-sail acceleration for Earth-bound mission design has been conducted only to a limited extent. A number of studies have investigated the effects of atmospheric drag on the sailcraft dynamics, though only treating drag as a perturbation or focusing on its use for drag-sailing applications [8–12]. Outside the context of drag-sailing, only a limited number of works consider the aerodynamic acceleration as an exploitable source of thrust. Among these are Refs. [13–15], which investigate aerodynamics-based optimal control laws for manoeuvring in the atmosphere, and the work by Carzana et al. [16], which provides a first-order analysis of the orbit-raising and inclination-changing capabilities of solar sails in low-Earth orbit. Similarly, research investigating the effects of PRP on the solar-sail dynamics and control is also limited. In particular, Refs. [7, 17, 18] present different models for the PRP acceleration and analyse its perturbing effect on the motion of Earth-bound sailcraft. The only work exploring PRP-based solar-sail control is by Barles [19], who, however, does so by employing a simplistic, low-fidelity dynamical model. In order to properly assess the manoeuvring capabilities of Earth-bound sailcraft, it is essential to incorporate the SRP, PRP, and aerodynamic accelerations in the solar-sail dynamics and trajectory design using high-fidelity models. To the authors' knowledge, no research has been conducted that accounts for the combined effect of these accelerations in the solar-sail trajectory design process. This research gap hinders the detailed design of Earth-bound sailcraft missions and the investigation into the potential of solar sailing for future Earth-bound mission applications.

This paper presents a solar-sail trajectory optimisation method that accounts for, and exploits, the sailcraft high-fidelity dynamics in the optimisation process. As an extension to the locally optimal steering laws developed by McInnes for ideal solar sails [1], this optimisation method allows to maximise the increase of any orbital element by taking into account not only the SRP acceleration, but also the PRP and aerodynamic accelerations. In this work, this optimisation technique is implemented by means of a grid-search-based algorithm. This paper describes the algorithm and its tuning which guarantees a high accuracy of the optimisation process. Finally, the trajectory optimisation method is exploited to fully characterise the manoeuvrability of Earth-bound sailcraft by studying their orbit-raising and inclination-changing capabilities in the near-Earth environment. To this aim, different large-scale parametric analyses are performed for a wide range of orbital regimes, solar activities, and sailcraft characteristics, taking NASA's recently launched ACS3 mission as baseline. The results of this work provide valuable insights into the manoeuvring capabilities of Earth-orbiting sailcraft, therefore supporting the mission design of future Earth-bound solar-sail missions for a variety of mission applications, such as active-debris removal and in-orbit servicing.

2. Dynamical Model

The dynamics of a solar sail in proximity of the Earth can be expressed within an Earth-centered inertial frame $I(x, y, z)$ with the x-axis lying on the Earth's equatorial plane and pointing towards the mean vernal equinox at 1st January 2000, the z-axis perpendicular to the equatorial plane and pointing towards the North Pole, and the y-axis completing the right-handed frame. Within this frame, the equations of motion can be expressed as:

$$\ddot{\boldsymbol{r}} = -\frac{\mu}{r^3}\boldsymbol{r} + \boldsymbol{a}_{\text{J2}} + \boldsymbol{a}_{\text{SRP}} + \boldsymbol{a}_{\text{PRP}} + \boldsymbol{a}_{\text{Aero}} \tag{1}$$

In Eq. (1), $\boldsymbol{r} = [x, y, z]^T$ is the sailcraft position vector, $r = \|\boldsymbol{r}\|$, $\mu = 398600.4415\,\text{km}^3/\text{s}^2$ is the Earth gravitational parameter [20], $\boldsymbol{a}_{\text{J2}}$ is the acceleration due to the Earth J_2 spherical harmonics coefficient, and $\boldsymbol{a}_{\text{SRP}}$, $\boldsymbol{a}_{\text{PRP}}$, and $\boldsymbol{a}_{\text{Aero}}$ are the SRP, PRP, and aerodynamic accelerations, respectively. In the following sections, the formal definitions of these accelerations and the reference sailcraft characteristics used throughout the remainder of the paper are presented.

2.1 J_2 Gravitational Acceleration

The Earth's J_2 gravitational acceleration is defined as:

$$\boldsymbol{a}_{\text{J2}} = -\frac{3}{2}\frac{R^2}{r^5}\mu J_2\left[(x\hat{\boldsymbol{x}} + y\hat{\boldsymbol{y}})\left(1 - 5\frac{z^2}{r^2}\right) + z\hat{\boldsymbol{z}}\left(3 - 5\frac{z^2}{r^2}\right)\right] \tag{2}$$

where $R = 6378.1363\,\text{km}$ is the Earth's radius [20], $J_2 = 1.082626925639 \cdot 10^{-3}$ is the Earth's J_2 gravitational field constant of the EGM2008 model [21], and $\hat{\boldsymbol{x}}$, $\hat{\boldsymbol{y}}$, and $\hat{\boldsymbol{z}}$ are the unit vectors pointing in the $I(x, y, z)$ frame's x-, y-, and z-axis directions, respectively.

2.2 Solar Radiation Pressure Acceleration

The SRP acceleration is modelled using the optical sail model devised by McInnes [1]. This model accounts for the reflection, absorption, and emission properties of the

sail, assuming that only the sail's frontside is exposed to sunlight. When using this model, the SRP acceleration is given by:

$$\boldsymbol{a}_{\text{SRP}} = \boldsymbol{a}_{\text{SRP},n} + \boldsymbol{a}_{\text{SRP},t} \tag{3}$$

where $\boldsymbol{a}_{\text{SRP},n}$ and $\boldsymbol{a}_{\text{SRP},t}$ are the acceleration components normal and tangential to the sail plane, respectively. These are defined as:

$$\begin{aligned}\boldsymbol{a}_{\text{SRP},n} = \nu\frac{a_c}{2}\big[&\left(1+\hat{r}_f s_f\right)\cos^2\alpha + \\ &\left(1-s_f\right)\hat{r}_f B_f \cos\alpha + \\ &\left(1-\hat{r}_f\right)\frac{\varepsilon_f B_f - \varepsilon_b B_b}{\varepsilon_f + \varepsilon_b}\cos\alpha\big]\,\hat{\boldsymbol{n}}\end{aligned} \tag{4}$$

$$\boldsymbol{a}_{\text{SRP},t} = \nu\frac{a_c}{2}\left(1-\hat{r}_f s_f\right)\cos\alpha\sin\alpha\,\hat{\boldsymbol{t}} \tag{5}$$

In Eqs. (4) and (5), a_c represents the solar-sail characteristic acceleration, that is, the maximum achievable SRP acceleration if the sail was perfectly reflecting. Its value provides a measure of the sailcraft thrusting performance and its definition is given by:

$$a_c = \frac{2S}{c\sigma} \tag{6}$$

where $S = 1361\,\text{W/m}^2$ is the solar flux at Earth [22], $c = 299792.458\,\text{km/s}$ is the speed of light in vacuum [23], and σ is the sailcraft mass-to-area ratio, also referred to as the loading parameter. In Eqs. (4) and (5), $\nu \in [0,1]$ denotes the shadow factor, which accounts for the effect of eclipses as per the conical shadow model of Ref. [24] and its value ranges from 0 (no sunlight reaches the sail) to 1 (sail completely illuminated). The angle $\alpha \in [0, \pi/2]$ represents the so-called solar-sail pitch angle measured between the instantaneous Sun-to-sailcraft direction, $\hat{\boldsymbol{s}}$ – also referred to as sunlight direction in the following – and the sail normal direction with positive component along $\hat{\boldsymbol{s}}$, $\hat{\boldsymbol{n}}$, see Fig. 1a. The direction $\hat{\boldsymbol{t}}$ represents the transversal direction defined as:

$$\hat{\boldsymbol{t}} = \hat{\boldsymbol{n}} \times \frac{\hat{\boldsymbol{s}} \times \hat{\boldsymbol{n}}}{\|\hat{\boldsymbol{s}} \times \hat{\boldsymbol{n}}\|} \tag{7}$$

Finally, the symbols r, s, B, and ε represent the reflectivity, specular reflection coefficient, non-Lambertian reflection coefficient, and emissivity of the sail, with the subscripts "f" and "b" indicating whether the optical coefficient refers to the front or back of the sail.

2.3 Planetary Radiation Pressure Acceleration

The PRP acceleration, $\boldsymbol{a}_{\text{PRP}}$, is modelled analytically as per the spherical sinusoidal model presented in Ref. [17]. This model assumes the Earth to be a spherical radiation source emitting radiation in two forms: the blackbody radiation emitted by the Earth itself, and albedo radiation, which represents the fraction of solar radiation reflected by the Earth. To represent the geographical distribution of the intensities of these radiations, the model assumes the blackbody radiation flux and albedo coefficient to vary sinusoidally with latitude. In addition, the intensity of the radiation incident on the sailcraft also depends on the sailcraft altitude, and, in the case of albedo radiation, the Sun-Earth-sailcraft geometrical configuration. Similar to the way the SRP acceleration varies with the pitch angle, the PRP acceleration varies with the so-called planetary pitch angle, $\alpha_\oplus$, measured between the radial and sail normal directions, see Fig. 1b. In particular, for $\alpha_\oplus$ values close to zero, the sail is oriented perpendicular to the radial direction, resulting in the largest magnitude of the $\boldsymbol{a}_{\text{PRP}}$ vector. Conversely, for $\alpha_\oplus$ values close to 90 deg, the sail is oriented edgewise to the radial direction and little PRP acceleration is produced. The spherical sinusoidal PRP acceleration model also accounts for the optical properties of the sail, although considering distinct

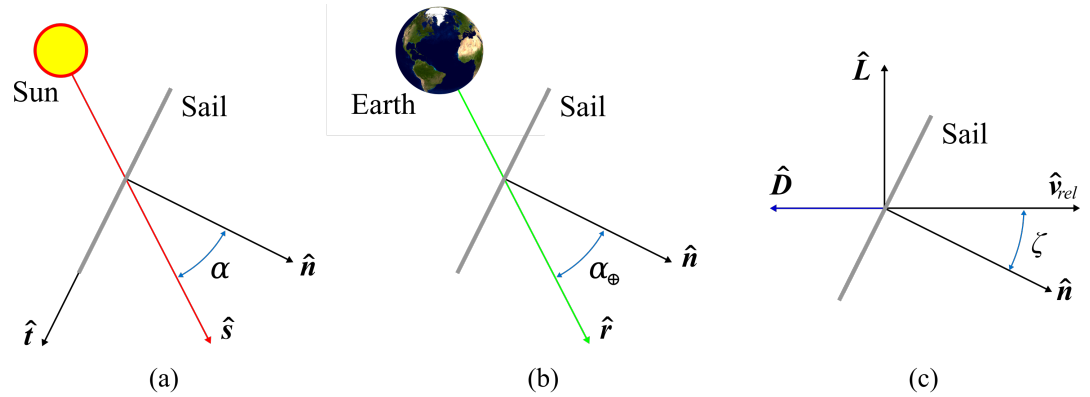

Fig. 1. Reference directions and attitude angles to compute the SRP (a), PRP (b), and aerodynamic (c) accelerations.

optical coefficients to compute the blackbody radiation pressure (BBRP) and albedo radiation pressure (ARP) accelerations, as blackbody radiation is primarily infrared radiation whereas albedo radiation is defined within the visible part of the spectrum, similar to solar radiation. A thorough mathematical description of the spherical sinusoidal PRP acceleration model is beyond the scope of this paper; the reader is referred to Refs. [7, 17] for further details.

2.4 Aerodynamic Acceleration

The sailcraft aerodynamics are modelled assuming the sail to behave as a flat plate in hyperthermal free-molecular flow conditions, in line with other works treating drag-perturbed solar-sail dynamics [13, 16, 25]. Under these assumptions, the aerodynamic acceleration is defined as:

$$\boldsymbol{a}_{\text{Aero}} = \frac{1}{2}\frac{\rho\, v_{rel}^2}{\sigma}\left(C_D\hat{\boldsymbol{D}} + C_L\hat{\boldsymbol{L}}\right) \tag{8}$$

where ρ is the atmospheric density, v_{rel} is the sailcraft relative velocity with respect to the atmosphere (assumed to be Earth-fixed), C_D and C_L are the drag and lift coefficients, respectively, and $\hat{\boldsymbol{D}}$ and $\hat{\boldsymbol{L}}$ are the drag and lift directions, respectively. In this paper, the atmospheric density is computed through an averaging method based on the NRLMSISE-00 model [26], as outlined in Ref. [16]. The underlying NRLMSISE-00 model is employed with solar radio flux at 10.7 cm and geomagnetic activity relative to the 50th percentile retrieved from the Marshall Space Flight Center's forecast of August 2024 [27]. The drag direction, $\hat{\boldsymbol{D}}$, points anti-parallel to the direction of the sailcraft relative velocity with respect to the atmosphere, $\hat{\boldsymbol{v}}_{rel}$, while the lift direction, $\hat{\boldsymbol{L}}$, points perpendicular to $\hat{\boldsymbol{v}}_{rel}$ and is coplanar with $\hat{\boldsymbol{n}}$ and $\hat{\boldsymbol{v}}_{rel}$, see Fig. 1c. The drag and lift coefficients are defined as:

$$\begin{aligned} C_D = 2\big[&\sigma_T + \sigma_N V_R|\cos\zeta| + \\ &(2-\sigma_N-\sigma_T)\cos^2\zeta\big]\,|\cos\zeta| \end{aligned} \tag{9}$$

$$C_L = 2\left[\sigma_N V_R + (2-\sigma_N-\sigma_T)\,|\cos\zeta|\right]\,|\cos\zeta|\sin\zeta \tag{10}$$

where σ_N and σ_T denote the normal and tangential momentum accommodation coefficient, respectively, V_R is the ratio of the average velocity of the atmospheric particles diffusively reflected by the sail and the sailcraft velocity, and $\zeta \in [0, \pi]$ represents the angle between $\hat{\boldsymbol{v}}_{rel}$ and $\hat{\boldsymbol{n}}$, see Fig. 1c.

2.5 Reference Sailcraft Specifics

This paper makes use of NASA's ACS3 mission as baseline for all analyses. ACS3 was launched on 23 April 2024 in a circular, Sun-synchronous orbit with the local time of the ascending node (LTAN) at 22:30 hrs and deployed its sail on 29 August 2024. Its specifics are given in Table 1 which will be used throughout the remainder of this paper, unless stated otherwise. In Table 1, $\boldsymbol{oc}_{vis}$ and $\boldsymbol{oc}_{IR}$ represent the sets of optical coefficients to compute the SRP and ARP accelerations (subscript "vis"), and BBRP acceleration (subscript "IR"), given in the following order: $[\hat{r}_f,\ s_f,\ \varepsilon_f,\ B_f,\ \hat{r}_b,\ s_b,\ \varepsilon_b,\ B_b]$.

Table 1. ACS3 sailcraft specifics.

Mass	16 kg
Area	80 m^2
σ	0.2 kg/m^2
a_c	$4.540 \cdot 10^{-2}$ mm/s^2
$\boldsymbol{oc}_{vis}$	[0.90, 0.82, 0.03, 0.79, 0.43, 0.53, 0.60, 2/3]
$\boldsymbol{oc}_{IR}$	[0.97, 0.82, 0.03, 0.79, 0.40, 0.53, 0.60, 2/3]
σ_N	0.8
σ_T	0.8
V_R	0.05

3. Optimization Method

The trajectory optimisation method used in this paper builds upon the locally optimal control theory developed by McInnes in Ref. [1], which allows to compute solar-sail steering laws to optimally increase any given orbital element. Similar to Ref. [1], the optimisation problem considered in this paper is defined as finding the optimal control vector $\boldsymbol{u}(t) = \hat{\boldsymbol{n}}(t)$ for which the cost function $J(\boldsymbol{u}(t)) = \dot{\text{æ}}(\boldsymbol{u}(t))$ is maximised at each moment in time, with æ denoting the orbital element of interest. When the Lagrange planetary equations are used to express $\dot{\text{æ}}$, the cost function assumes the following form [1]:

$$J(\boldsymbol{u}(t)) = \dot{\text{æ}}(\boldsymbol{u}(t)) = \boldsymbol{\lambda}^T \cdot \boldsymbol{a}(\boldsymbol{u}(t)) \tag{11}$$

where $\boldsymbol{a}$ is the sum of all accelerations acting on the sail and $\boldsymbol{\lambda}$ is the so-called primer vector, whose direction $\hat{\boldsymbol{\lambda}}$ represents the instantaneous optimal thrust direction to maximise the orbital element's rate of change. Equation (11) highlights that, in order to maximise $\dot{\text{æ}}$, the sailcraft should be oriented in a way that produces the largest acceleration component along $\hat{\boldsymbol{\lambda}}$. It should be noted that the acceleration term $\boldsymbol{a}$ includes, among others, gravitational accelerations, but that these are independent of the sailcraft attitude control $\boldsymbol{u}(t) = \hat{\boldsymbol{n}}(t)$. Therefore, gravitational accelerations do not affect the optimisation problem and the acceleration term $\boldsymbol{a}$ can be considered, without loss of generality, as the sum of only the *attitude-dependent* accelerations acting on the sail.

The exact expression for $\boldsymbol{a}$ depends on the solar-sail dy-

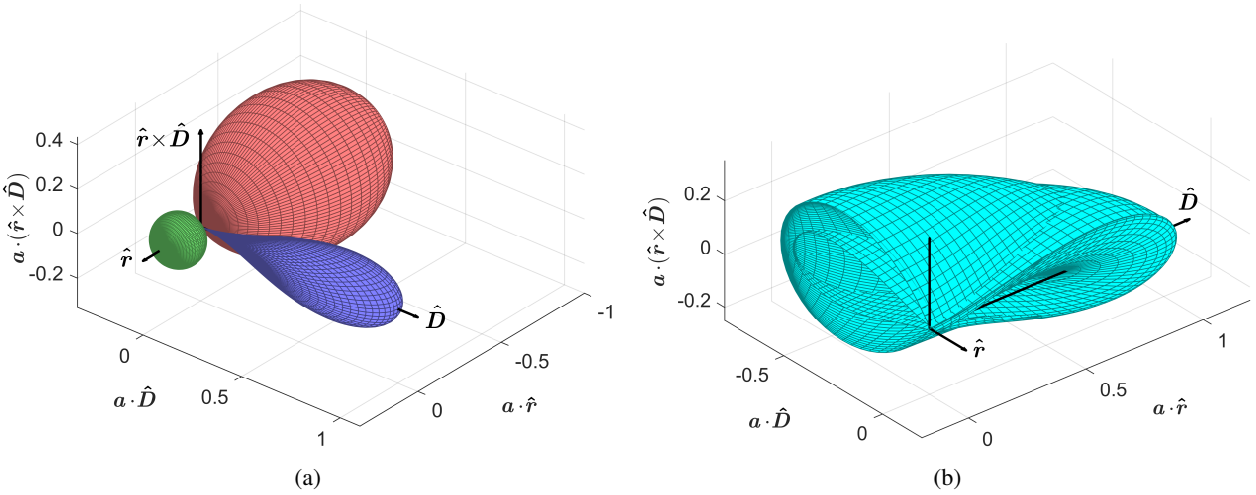

Fig. 2. Acceleration envelope surfaces of (a) the SRP, PRP, and aerodynamic accelerations (in red, green, and blue, respectively) and (b) the resulting total acceleration.

namics under consideration and it largely affects the complexity of the optimisation problem. As demonstrated by McInnes [1], when considering a perfectly reflecting solar sail subject only to SRP, $J(\boldsymbol{u}(t))$ assumes a simple form which allows for an analytical solution to the optimal control problem. Conversely, Carzana et al. [16] showed that, when adding the effect of aerodynamics, an analytical solution no longer exists, therefore requiring the use of numerical methods. In this paper, the acceleration term $\boldsymbol{a}$ accounts for the optical properties of the sail and the combined effect of SRP, PRP, and aerodynamics, as per the high-fidelity dynamical model presented in Section 2. In order to visualise the complexity of the optimisation problem associated with these dynamics, Figure 2a displays the so-called acceleration envelope (AE) surfaces of the SRP, PRP, and aerodynamic accelerations, that is, the sets of all possible SRP, PRP, and aerodynamic accelerations achieved by varying the sailcraft's attitude. The plot illustrates an example scenario in which the sunlight direction, $\hat{\boldsymbol{s}}$, is perpendicular to the drag direction, $\hat{\boldsymbol{D}}$, and anti-parallel to the radial direction, $\hat{\boldsymbol{r}}$. Also, the maximum SRP and aerodynamic accelerations are of the same magnitude, while the maximum PRP acceleration is 25% of that. As will be discussed in Section 3.1, scenarios like this can occur for sailcraft flying in low Earth orbit, in proximity of the subsolar point. When the SRP, PRP, and aerodynamic accelerations are summed, the resulting total AE surface assumes the highly nonlinear, self-intersecting shape illustrated in Figure 2b. In the context of the optimisation problem at hand, maximising $J(\boldsymbol{u}(t))$ is equivalent to determining the point of this AE surface that is tangent to a plane orthogonal to $\hat{\boldsymbol{\lambda}}$. This task is rendered difficult by the non-convex shape of the AE surface and the fact that it features sharp edges, see Fig. 2b. Indeed, on the one hand, the non-convex shape of the AE surface makes small variations in the orientation of the above-mentioned plane able to completely change the tangent point on top of the AE surface. On the other hand, the presence of sharp edges renders the tangency problem degenerate. The combination of these two effects therefore makes the optimal attitude very sensitive to the $\hat{\boldsymbol{\lambda}}$ direction. Furthermore, it should also be noted that the shape of the AE surface and the $\hat{\boldsymbol{\lambda}}$ direction vary over time with the instantaneous state of the sailcraft, thereby adding additional complexity to the problem.

Similar to Ref. [16], the complexity of the above-presented optimisation problem impedes the existence of an analytical resolution. Therefore, in this paper, the optimisation is performed numerically using a grid-search method. Specifically, for each integration step of the trajectory propagation, the $\hat{\boldsymbol{\lambda}}$ direction is computed analytically through the Lagrange planetary equations, whereas the total AE surface of Fig. 2b is found by computing the acceleration vectors corresponding to a mesh of sail normal directions evenly spaced with an angular step $d\Lambda$ within the azimuth-elevation spherical coordinate domain $[0, 2\pi] \times [-\pi/2, \pi/2]$. For each of these acceleration vectors $\boldsymbol{a}$ that collectively define the AE surface, the cost function J is evaluated using Eq. (11). Finally, the sail normal direction corresponding to the maximum value of J is taken as the (locally) optimal sail normal direction.

Because the angular step $d\Lambda$ affects the number of points used to represent the AE surface, tuning of $d\Lambda$ is required to ensure a high accuracy of the optimal solution.

In view of this, Section 3.1 presents an analysis of the accelerations experienced by solar sails in the near-Earth environment. This analysis is performed to determine the most complex scenario to consider for the tuning of $d\Lambda$, which is performed in Section 3.2.

It should be noted that the optimisation method outlined in this section will be used in the remainder of the paper to maximise the rates of change of semi-major axis, a, and inclination, i. Since orbital altitude is defined as $h = (a - R)$ in this paper, changes in semi-major axis correspond to changes in altitude. Therefore, the altitude rate of change will be considered the optimisation objective for the orbit-raising steering law without loss of generality, and increases in semi-major axis will be referred to as altitude gains.

3.1 Accelerations Experienced by Sailcraft in Earth Orbit

The analysis in this section considers the ACS3's mission parameters given in Table 1 and a simulation start date of 20 March 2027. This date corresponds to the spring equinox, so the Earth-to-Sun direction is aligned with the positive x-axis direction of the $I(x, y, z)$ frame and the subsolar point lies on the Earth's equator. Furthermore, the year 2027 is considered because the solar activity in 2027 is expected to be of medium intensity [27]. In order to analyse the near-Earth dynamical environment, the maximum achievable SRP, BBRP, ARP, and aerodynamic accelerations have been computed for a wide variety of sailcraft positions across the (x, z) plane up to altitudes of 5000 km. The (x, z) plane is coplanar with the direction of the Earth's polar axis and the Earth-Sun direction, thereby allowing to easily observe how eclipses and variations in the albedo coefficient and the blackbody radiation flux affect the dynamics. Given the maximum SRP, BBRP, ARP, and aerodynamic accelerations at each sailcraft location, the regions around the Earth wherein different types of accelerations dominate the dynamics can now be determined. In particular, at each sailcraft location, the largest of the aforementioned accelerations is recorded together with any other acceleration that is at least 5% of this largest acceleration component.

Figure 3 shows the dominating accelerations as a function of the sailcraft altitude, h, and polar angle measured from the $\hat{x}$ (Earth-Sun) direction, θ. To enhance visual interpretation of the results, the results are displayed in an Earth-centered polar plot with an altitude grid spacing of 1000 km, see Fig. 3a, and a Cartesian plot with the maximum altitude restricted to 2000 km, see Fig. 3b. The plots show that three macro-regions exist which exhibit different patterns: 1) the sunlit region in proximity of the subsolar point (around $\theta = 0$ deg), 2) the eclipse region

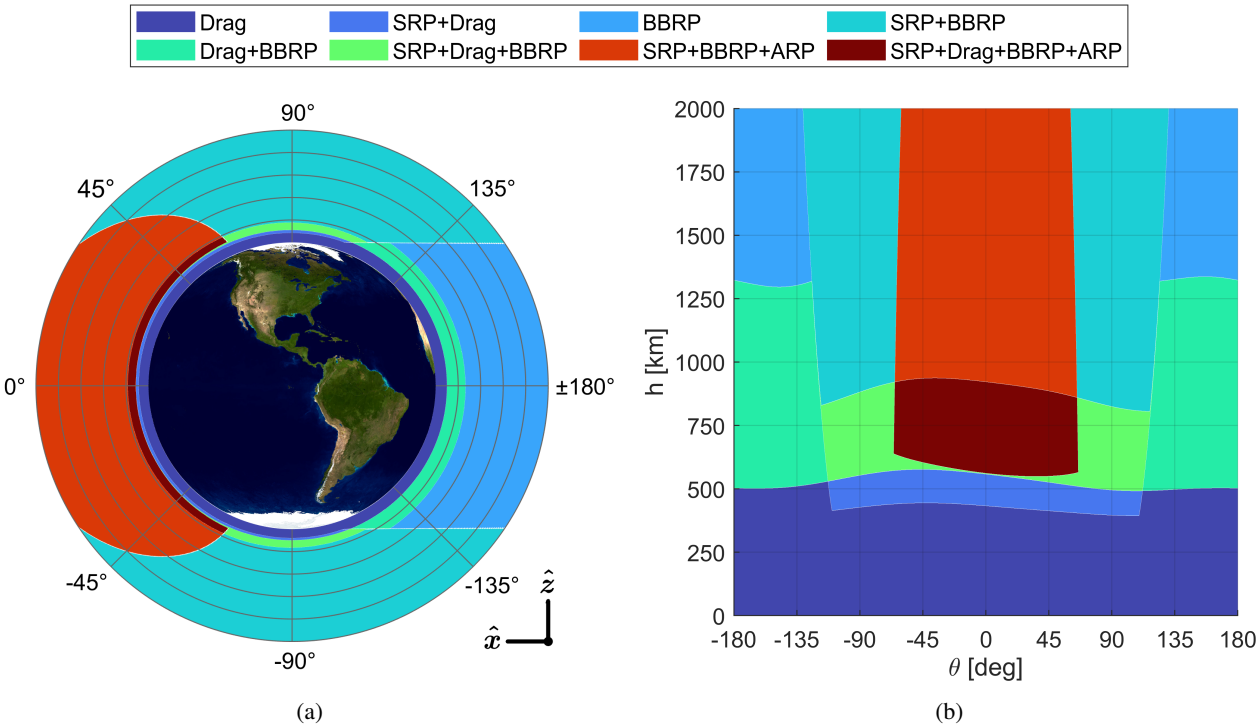

(a) (b)

Fig. 3. Accelerations dominating the solar-sail dynamics around Earth: (a) polar plot and (b) Cartesian plot.

(around $\theta = 180$ deg), and 3) the region situated between these two, centered around the poles (around $\theta = \pm 90$ deg).

In the eclipse region, the only accelerations present are those from atmospheric drag and BBRP. Drag is especially strong for altitudes below 500 km, rendering the BBRP acceleration negligible in comparison. However, for increasing altitudes, the acceleration due to drag decreases more rapidly than the acceleration due to BBRP. Therefore, the BBRP acceleration becomes increasingly more relevant, eventually reaching magnitudes comparable to that of drag or even superior to it, particularly for altitudes above 1300 km.

In proximity of the poles, the SRP acceleration affects the dynamics significantly, in particular above 400 km. Similar as for the eclipse region, drag decreases rapidly with altitude, rendering it negligible for altitudes above 800-900 km, where the SRP and BBRP accelerations are the dominating accelerations. It should be noted that, close to the poles, also ARP influences the sailcraft motion. However, because the sunlight reflection angle with the Earth surface is large, the ARP acceleration magnitude is small, therefore affecting the dynamics only to a negligible extent.

Finally, the region in proximity of the subsolar point is the most dynamically complex, as in this case ARP also has a considerable effect on the dynamics. Its relative magnitude as compared to the other accelerations is particularly large above 500 km which, crucially, results in a region in which all accelerations significantly affect the dynamics. This region is confined to, approximately, an altitude range of $[550, 950]$ km and a θ (latitude) range of $[-65, 65]$ deg. This region provides the starting point for the tuning of the grid-search angular step performed in the next section.

3.2 Grid-search Angular Step Tuning

This section presents an analysis to tune the value of the grid-search angular step, $d\Lambda$, by assessing how changes in this value affect the accuracy of the grid-search optimisation. To this aim, the dynamics presented in Section 2 have been propagated while employing the grid-search optimisation method for different values of $d\Lambda$ in order to maximise either the change in orbital altitude or inclination. The simulation start date has again been set to 20 March 2027 and a simulation duration of one day has been considered. This time, the initial orbital elements correspond to a circular, Sun-synchronous orbit with an altitude of 750 km and an LTAN of 12:00 hrs. By using this set of orbital elements, the sailcraft flies through the highly perturbed region identified in Section 3.1 once per orbit. This renders the sailcraft motion highly sensitive to the control optimisation, thus making this test scenario particularly suited for tuning $d\Lambda$. For each optimisation objective, the trajectory optimisations have been performed using the $d\Lambda$ values $\{5,\ 2,\ 1,\ 0.5,\ 0.2,\ 0.1,\ 0.01\}$ deg. Then, for each propagation, the following relative error has been computed:

$$\varepsilon_{rel} = \frac{\Delta\text{œ} - \Delta\text{œ}_{ref}}{\Delta\text{œ}_{ref}} \tag{12}$$

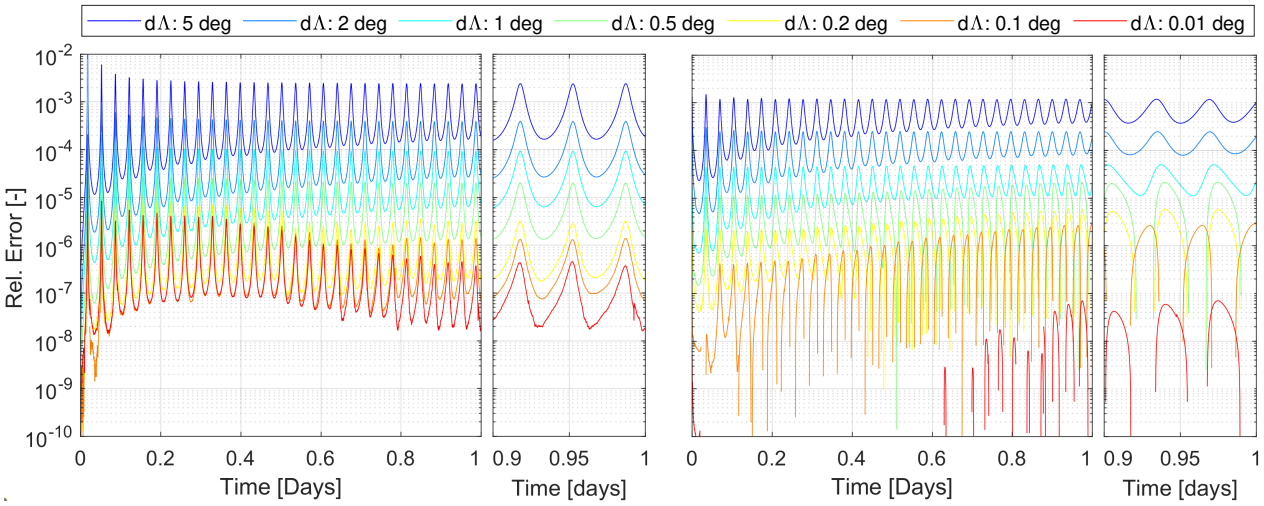

(a) (b)

Fig. 4. Relative errors in altitude (a) and inclination (b) change for different grid-search angular steps, $d\Lambda$.

where $\Delta\text{æ}$ is the gain in altitude or inclination achieved for a given value of $d\Lambda$, and $\Delta\text{æ}_{ref}$ is the same gain obtained by a reference, high-accuracy solution found for $d\Lambda = 0.001$ deg.

Figures 4a and 4b present the variation in ε_{rel} over time for the selected values of $d\Lambda$, for the orbit-raising and inclination-changing steering laws, respectively. The relative error shows an oscillating trend for both steering laws, regardless of the value for $d\Lambda$. This trend is due to the J_2 gravitational acceleration, which, although it does not yield any secular variation in the semi-major axis and inclination, it produces short-term periodic fluctuations in these orbital elements. Figure 4a shows that, even for a large angular step of $d\Lambda = 5$ deg, only small relative errors appear in the semi-major axis change after one day, with ε_{rel} in the order of 10^{-3}. Decreasing $d\Lambda$ results in a consistent, steady reduction of this error, which gets as small as 10^{-7} for $d\Lambda = 0.01$ deg.

For the inclination-changing case in Fig. 4b, the error curves appear truncated at certain time intervals for $d\Lambda$ values smaller than 1 deg. This suggests that ε_{rel} becomes negative and the reference solution performs *worse* than the solution tested, see Eq. (12). Further investigation showed that this result is due to a second-order effect introduced when employing a slightly different value of $d\Lambda$ compared to the reference solution. Then, the J_2-induced short-term oscillations in the inclination of the tested solution and reference solution go out of phase. Consequently, for some time intervals, the inclination of the tested solutions appear larger than that of the reference solution, resulting in a negative ε_{rel}.

To ensure a high accuracy of the optimisation routine, a maximum relative error tolerance of 10^{-4} is selected. This value is chosen based on the accuracy of the averaged NRLMSISE-00 atmospheric density model presented in Section 2.4, which yields maximum relative errors at most in the order of 10^{-3}, see Ref. [16]. Therefore, in order not to compound this error, a threshold that is ten times smaller was selected. The largest angular step for which $\varepsilon_{rel} < 10^{-4}$ at the end of the one-day propagation is $d\Lambda = 1$ deg for both steering laws. Consequently, this $d\Lambda$ value will be used in the remainder of this paper.

4. Analysis of the Solar-sail Manoeuvring Capabilities

This section presents three sensitivity analyses designed to investigate the manoeuvrability of Earth-orbiting solar sails. Specifically, the sensitivity analyses explore the effects of the PRP acceleration, solar activity intensity, and sailcraft characteristic acceleration on the orbit-raising and inclination-changing capabilities of Earth-bound sailcraft, for a wide variety of orbits with different altitudes and LTANs. The common and analysis-dependent settings used for the sensitivity analyses are detailed in Tables 2 and 3, respectively, and they are presented hereinafter.

All sensitivity analyses consider the dynamics presented in Section 2, which have been propagated for one day while employing the grid-search optimal control method to maximise the altitude or inclination increase. Based on the angular step tuning performed in Section 3.1, the grid-search optimisation has been implemented with an angular step $d\Lambda = 1$ deg. For each steering law, several initial orbits have been considered, specifically, circular, Sun-synchrounous orbits with altitudes varying between 300 km and 1000 km with a step size of 50 km and LTANs spaced by one hour along the entire 24-hour time span. Because the Sun-synchrounous inclination depends on altitude, its value varies almost linearly between 96.672 deg at 300 km and 99.479 deg at 1000 km. As indicated in Table 3, depending on the sensitivity analysis under consideration, the optimisation routine described in Section 3 has been performed including or excluding the PRP acceleration from the optimisation process, that is, including or excluding the contribution of $\boldsymbol{a}_{PRP}$ from the cost function's acceleration term, $\boldsymbol{a}$, see Eq. (11). Depending on the sensitivity analysis, different simulation start dates have been considered as well, namely, 20 March 2024, 2027, and 2031. These dates correspond to maximum, medium, and minimum solar activity intensities, respectively, as forecasted by the Marshall Space Flight Center in August 2024 [27]. Furthermore, because these dates correspond to spring equinoxes, the Sun is approximately in the Earth's equatorial plane throughout the simulations. Finally, the ACS3 solar-sail specifics given in Table 1 have been used for all sensitivity analyses, except for the characteristic acceleration, a_c. Indeed, by referring to the characteristic acceleration of ACS3 as a_c^{ref}, characteristic accelerations of $a_c^{ref}/10$, a_c^{ref}, or $10a_c^{ref}$ have been used, depending on the sensitivity analysis under consideration.

The sensitivity analyses and their results are discussed in the following sections. For the sake of clarity in the treatment, it should be noted that the term "parametric analysis" will be used hereinafter when referring to an analysis performed by iterating over the parameters of Table 2, i.e., when considering different steering laws, initial orbital altitudes and LTANs. In accordance with this terminology, a *sensitivity* analysis consists of a number of *parametric* analyses, each considering a different solar activity intensity, sailcraft specifics, or optimisation specifics, as outlined in Table 3.

Table 2. Common settings to all sensitivity analyses of Section 4.

Steering Law	Orbit-raising, Inclination-changing
Orbit Type	Circular + Sun-synchronous
Sim. Duration	1 day
Altitudes	300, 350, 400, ..., 1000 km
LTANs	00:00, 01:00, 02:00, ..., 23:00 hrs

Table 3. Analysis-dependent settings used for the sensitivity analyses of Section 4.

Analysis	Ref. Scenario	Effect of $\boldsymbol{a}_{PRP}$	Effect of Solar Activity	Effect of a_c
Section	4.1	4.2	4.3	4.4
$\boldsymbol{a}_{PRP}$ Optimised	Yes	Yes, No	Yes	Yes
Sim. Start Date (Solar Activity)	20 Mar 2027 (Medium)	20 Mar 2027 (Medium)	20 Mar 2024, 2027, 2031 (Maximum, Medium, Minium)	20 Mar 2027 (Medium)
Sailcraft Specs	ACS3*	ACS3*	ACS3*	ACS3* with a_c equal to $a_c^{ref}/10,\ a_c^{ref},\ 10\,a_c^{ref}$

* See Table 1

4.1 Reference Scenario

The parametric analysis presented in this section aims to assess the manoeuvring capabilities of ACS3 under the reference conditions (see Table 3), that is, assuming a medium solar activity intensity, including PRP in the optimisation process, and assuming the characteristic acceleration of ACS3.

Figure 5a shows the results for the orbit-raising case by illustrating the altitude gain achieved after one day, Δh, as function of the initial orbital altitude, h, and LTAN. As can be seen, for altitudes below 500-550 km, little to no altitude increase can be achieved. This is because aerodynamic drag is particularly strong in this region – as evidenced also in Fig. 3 – which prevents the sailcraft from gaining altitude. For higher altitudes, atmospheric density decreases rapidly and with it also aerodynamic drag. This yields better orbit-raising capabilities and increasingly larger altitude gains, particularly for LTANs close to $06:00$ and $18:00$ hrs. These LTANs correspond to dawn-dusk orbits, for which the sailcraft never enters the Earth's eclipse region, allowing the sailcraft to exploit SRP at all time, leading to large altitude gains. On the other hand, for LTANs close to 00:00 and 12:00 hrs, the sailcraft orbits in a noon-midnight orbit and is shadowed by Earth for a prolonged section of the orbit (approximately 33% to 40%, depending on the altitude). Even though this affects the orbit-raising capabilities negatively compared to the dawn-dusk case, the impact on the altitude gain is relatively limited. This is due to the fact that, for noon-midnight orbits, the sailcraft passes over the subsolar point once per orbit, where albedo radiation is particularly strong. Consequently, the ARP acceleration can be exploited more effectively, partially counteracting the decrease in performance due to the presence of eclipses.

Similar to Fig. 5a, Fig. 5b shows the inclination gain achieved after one day, Δi, when implementing the inclination-changing steering law for different combinations of initial altitude, h, and LTAN. The results show that the largest inclination changes are achieved at low altitudes. At low altitudes, the sail can exploit aerodynamic lift by orienting itself at a non-zero angle of attack to produce a large out-of-plane acceleration and thereby an inclination gain. Nevertheless, this sailcraft attitude also produces considerable drag, which makes the sailcraft lose altitude rapidly. Consequently, for altitudes below 450 km, the sailcraft deorbits in less than one day, which is represented with the white region in the plot. Increasing the altitude results in smaller aerodynamic forces and a swift decrease in the inclination gain until an altitude of $h = 600$ km. Beyond $h = 600$ km, the inclination gain shows only a weak dependency on altitude, indicating that the aerodynamic acceleration is no longer dominant – as evidenced also by Fig. 3; any inclination change is primarily achieved by exploiting SRP and PRP. For altitudes $h > 600$ km, larger inclination gains are found for LTANs around 06:00 and 18:00 hrs, reaching values up to 0.01 deg. This result is due to the favourable relative orientation of the sunlight direction with respect to the orbital

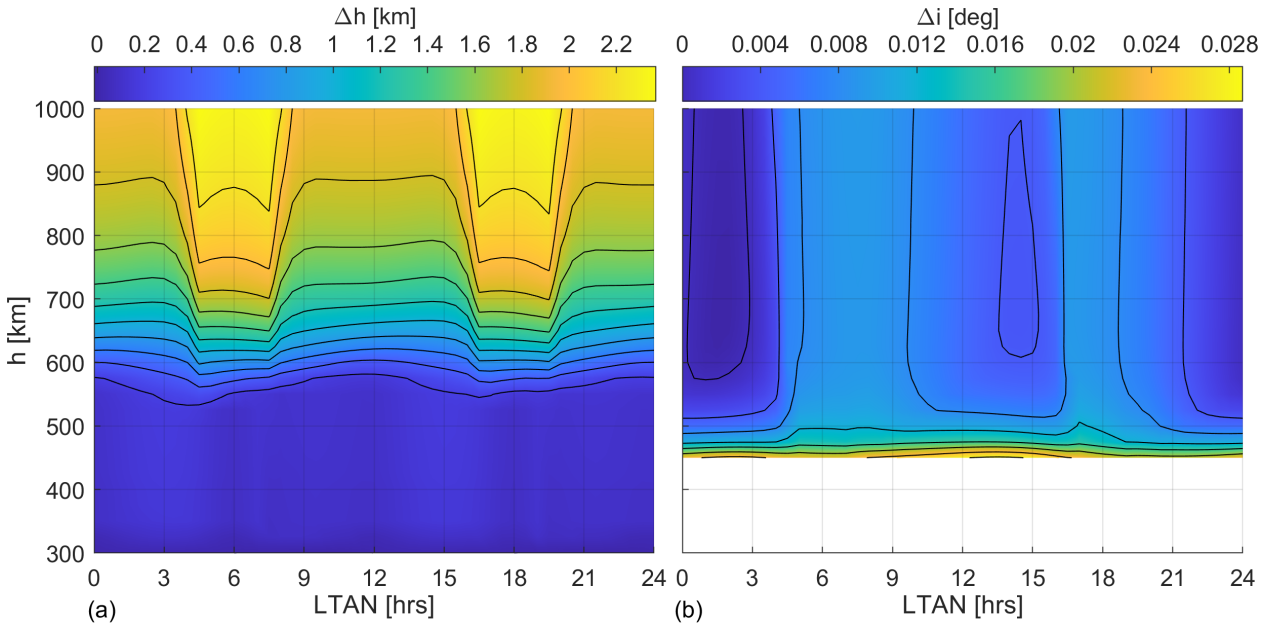

Fig. 5. Altitude (a) and inclination (b) gains obtained for the reference scenario.

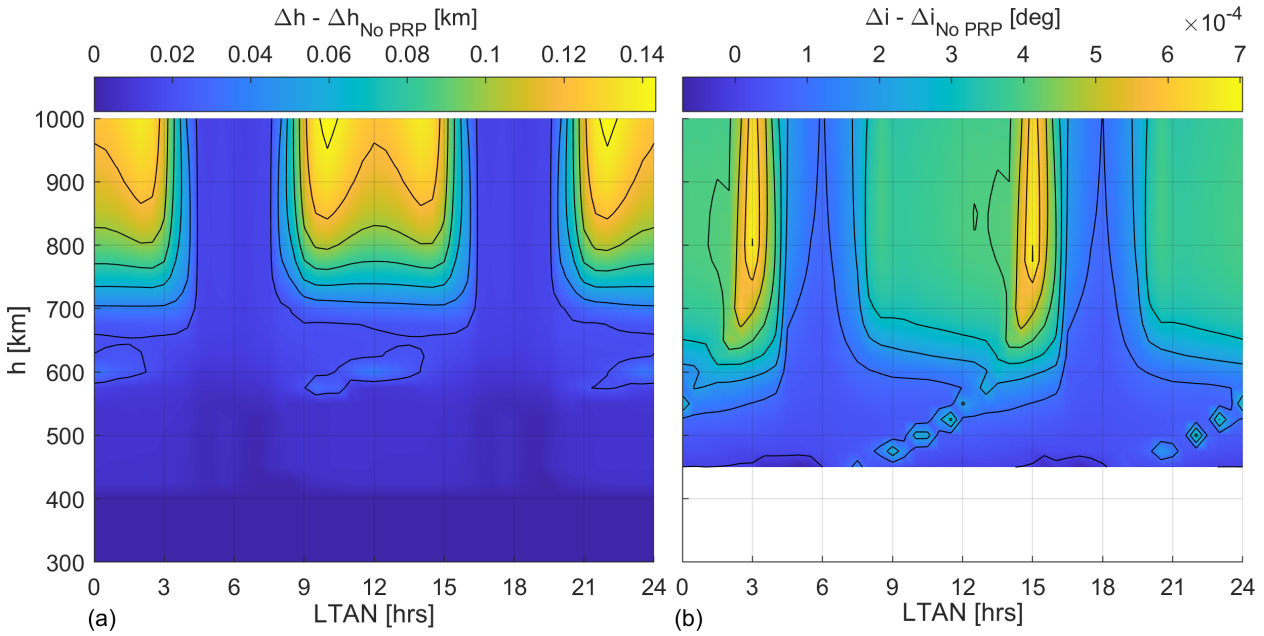

Fig. 6. Difference between the altitude (a) and inclination (b) gains for the PRP-based and no-PRP optimisations.

plane, which enables the sailcraft to generate larger out-of-plane accelerations.

4.2 Analysis on the Effect of Planetary Radiation Pressure

The parametric analysis presented in this section investigates to what extent the PRP acceleration can be exploited to enhance the solar-sail manoeuvring capabilities around Earth. To this aim, the same analysis as in Section 4.1 is conducted, except that the PRP acceleration is now only accounted for in the dynamics and not in the optimisation process, see Table 3.

Figure 6a shows the results for the orbit-raising case, displaying the signed difference between the altitude gains

obtained by including and excluding the PRP acceleration in the optimisation process, denoted as $\Delta h - \Delta h_{\text{NoPRP}}$. Predictably, the difference is always positive indicating that if the PRP acceleration is not accounted for in the optimisation, it acts as a perturbation and negatively affects the altitude gain, regardless of the orbit considered. The plot shows that neglecting PRP in the optimisation has a minor effect on the altitude increase for LTANs around $06:00$ and $18:00$ hrs but a significant impact for orbits with LTANs close to 00:00 and 12:00 hrs. Indeed, incorporating the PRP acceleration in the optimisation can result in altitude gains that are up to 10% larger than those found by the no-PRP optimisation. As discussed in Section 4.1, the increased orbit-raising capabilities achieved for noon-midnight orbits are a direct consequence of the large ARP the sailcraft experiences and exploits for manoeuvring.

Similar to Fig. 6a, Fig. 6b illustrates the signed difference between the inclination gains obtained by including and excluding the PRP acceleration in the optimisation process, denoted as $\Delta i - \Delta i_{\text{NoPRP}}$. The plot shows that the PRP acceleration can be particularly exploited for altitudes above 700 km and for LTANs in a narrow band around 03:00 and 15:00 hrs. For these LTANs, the sailcraft passes close to the subsolar point where the direction of the relatively large ARP acceleration can optimally contribute to the optimal thrust direction, $\hat{\boldsymbol{\lambda}}$. This enables inclination changes 10% to 20% larger than when PRP is not accounted for in the optimisation. The benefit of exploiting PRP is lost when slightly larger LTANs at 06:00 and 18:00 hrs are considered. Indeed, these LTANs correspond to dawn-dusk orbits for which the ARP acceleration is almost zero. The plot also shows that, for LTANs between 08:00 and 14:00 hrs and between 20:00 and 02:00 hrs, PRP can be exploited to some extent and with an almost constant effectiveness. Finally, it is interesting to note that, for very low altitudes and specific LTANs, the difference between the PRP-based and no-PRP inclination gains assumes negative values. This is because the trajectory found by the no-PRP optimisation can yield a faster altitude decrease than the PRP-based optimisation, thereby inducing a larger lift and greater inclination gain towards the end of the simulation.

4.3 Analysis on the Effect of Solar Activity

The sensitivity analysis presented in this section aims to investigate the influence of solar activity on the manoeuvrability of solar sails in Earth orbit. For this purpose, the parametric analysis in Section 4.1, valid for medium-intensity solar activity, has been repeated using two different simulation start dates that correspond to solar minimum and maximum conditions, see Table 3.

Figure 7 shows three contour plots illustrating the achievable altitude gains after one day, Δh, for minimum, medium, and maximum solar activities. It should be noted that, since the results for the medium solar activity conditions correspond to those presented in Section 4.1, the plots in Fig. 7b and 5 coincide. Still, Fig. 7b was included here to facilitate a comparison with the results obtained for solar minimum and maximum conditions. For stronger solar activities, the contour lines gradually shift towards higher altitudes, which indicates that the orbit-raising performance decreases with solar activity intensity. The plots show that this reduction in orbit-raising capabilities is particularly pronounced at lower altitudes, where aerodynamic drag is stronger. This can be appreciated by noting that the region for which $\Delta h < 0.2$ km, that is, the region for which orbit raising is proven particularly challenging, extends rapidly for increasing solar activity. This region shifts from initial altitudes up to 450 km for solar minimum conditions to initial altitudes up to 600 km for solar maximum conditions, in agreement with similar results found in the literature [16]. For higher initial orbital altitudes, h, atmospheric drag affects the sailcraft dynamics increasingly less and, therefore, the influence of solar activity is less noticeable. In the plots, this can be observed by the fact that for high altitudes fewer contour lines are given and, at the same time, the achievable Δh gains are approximately the same regardless of the solar activity.

Figure 8 provides the results for the inclination-changing case, showing the achievable inclination gains after one day, Δi, for different solar activity intensities. Similar to the orbit-raising case, a stronger solar activity results in stronger drag and a higher minimum altitude for which manoeuvring is possible. Passing from solar minimum to solar maximum conditions, the minimum altitude gradually shifts from 400 to 500 km, as highlighted by the white regions in the plots. Figure 8 also shows that, for altitudes above 600 km, the achievable inclination gains become almost independent of the solar activity. This is due to the fact that, when outside the high-density region of the atmosphere, inclination change is obtained by exploiting primarily the SRP and PRP accelerations rather than aerodynamic acceleration. Consequently, the results are less affected by the intensity of the solar activity and atmospheric drag.

4.4 Analysis on the Effect of Characteristic Acceleration

The sensitivity analysis presented in this section investigates the influence of the characteristic acceleration, a_c, on the manoeuvring capabilities. The characteristic acceleration is a measure of the achievable thrusting performance of a sailcraft and changes in its value affect the achievable SRP, PRP, and aerodynamic accelerations in

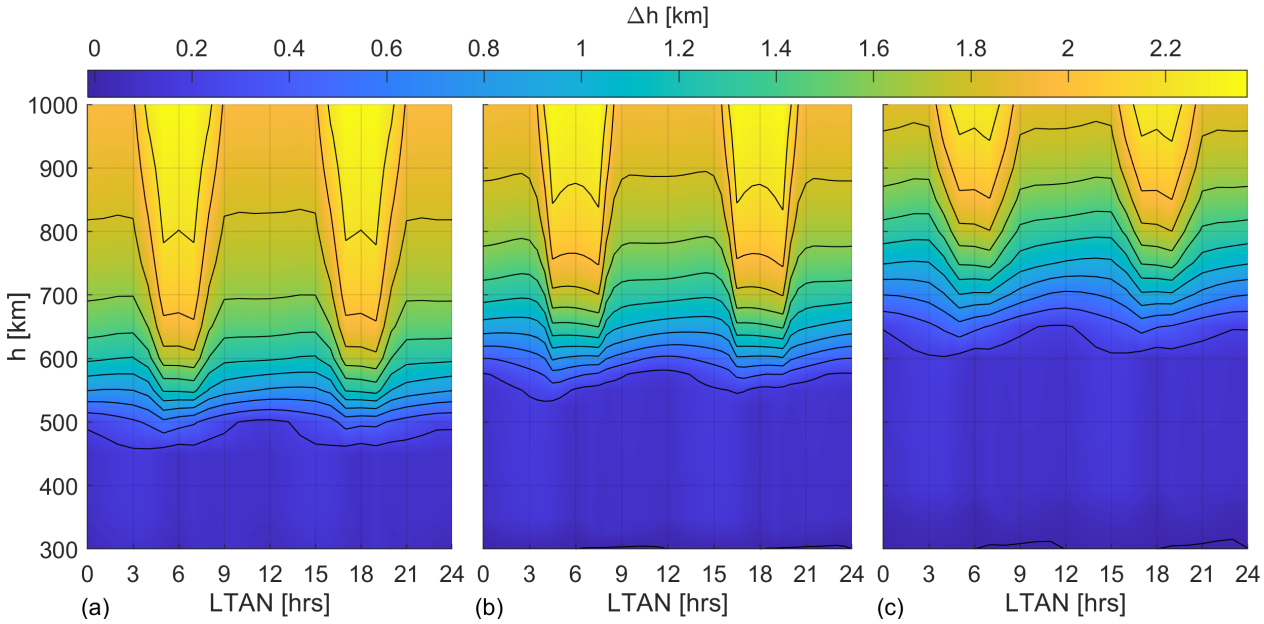

Fig. 7. Altitude gains obtained for solar activities of minimum (a), medium (b), and maximum (c) intensity.

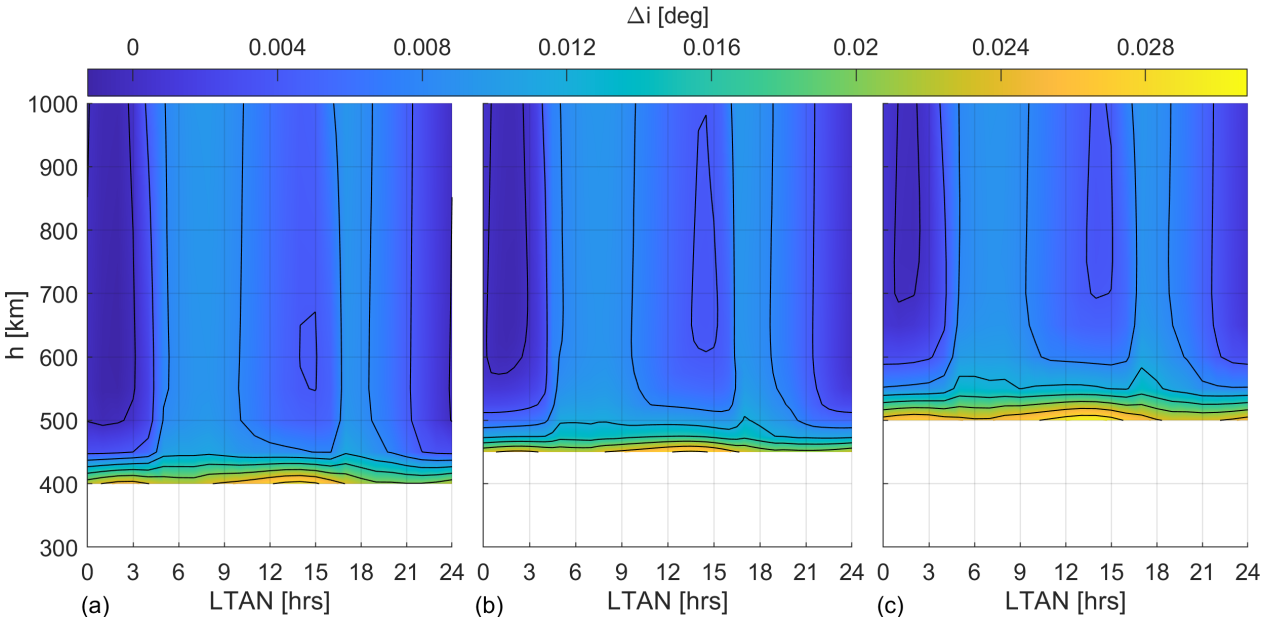

Fig. 8. Inclination gains obtained for solar activities of minimum (a), medium (b), and maximum (c) intensity.

a linear manner. To investigate the impact of the characteristic acceleration on the sailcraft's manoeuvrability, the parametric analysis presented in Section 4.1 has been repeated using two different values for a_c equal to either $1/10$ or 10 times the characteristic acceleration of ACS3, a_c^{ref}, see Table 3.

Figure 9 displays the results for the orbit-raising case showing the contour plots of the achievable altitude gains after one day, Δh, for each of the three characteristic accelerations. It should be noted that, since the results for $a_c = a_c^{ref}$ correspond to those presented in Section 4.1, the plots in Fig. 9b and 5 coincide. Nevertheless, this plot was included also in Fig. 9 to facilitate a comparison with the results obtained for $a_c = a_c^{ref}/10$ and $a_c = 10a_c^{ref}$. Figure

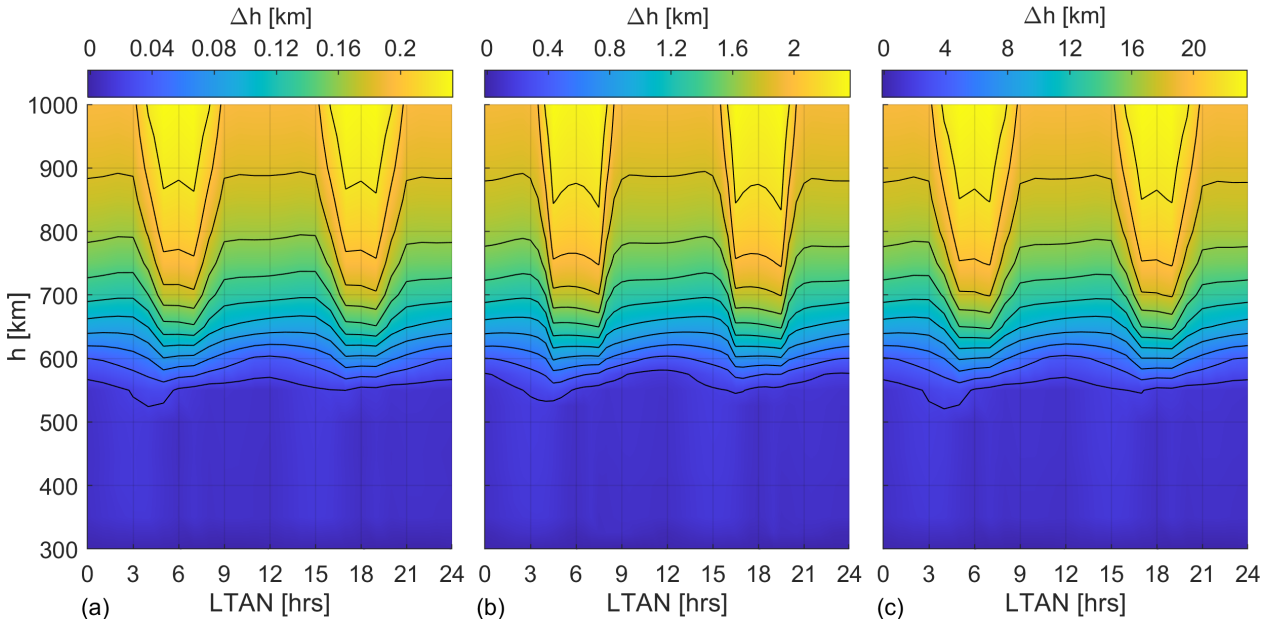

Fig. 9. Altitude gains obtained for characteristic accelerations ten times larger (a), equal (b), and ten times smaller (c) than that of ACS3.

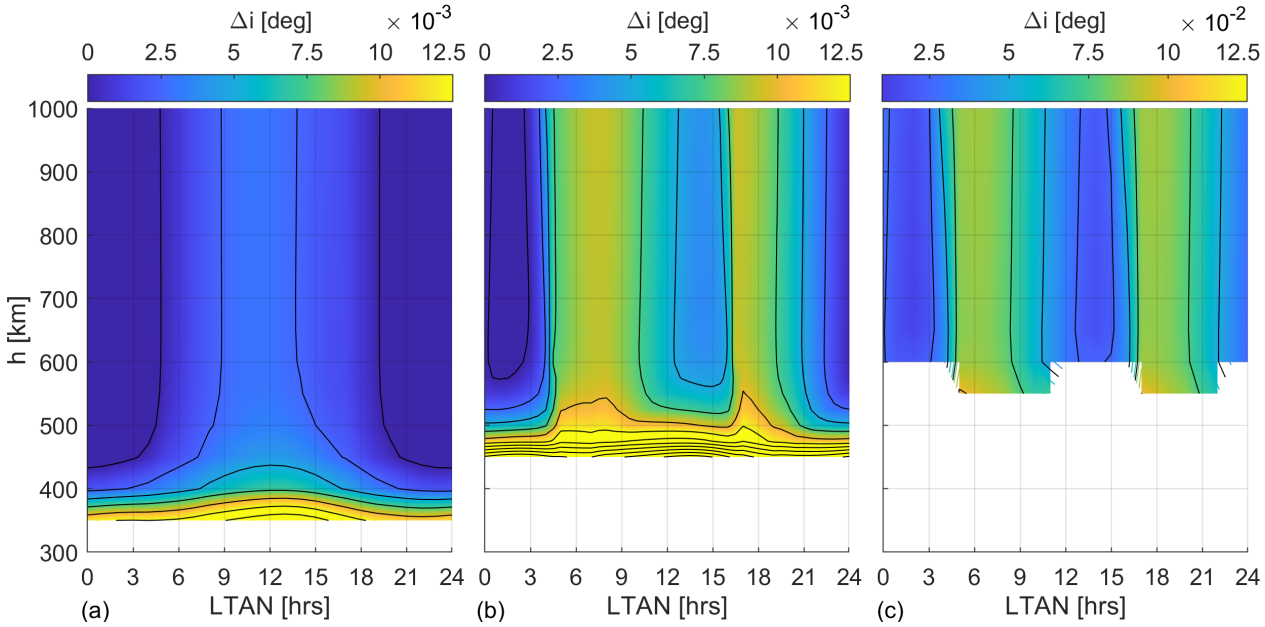

Fig. 10. Inclination gains obtained for characteristic accelerations ten times larger (a), equal (b), and ten times smaller (c) than that of ACS3.

9 shows that the way in which Δh varies with the initial altitude and LTAN is nearly identical for all characteristic accelerations considered. However, the magnitudes of the achievable Δh gains get scaled in a linear manner with a_c, as can be observed from the different limits for the colourbars for each of the plots in Figure 9. On the one hand, this result is a consequence of the proportionality of $\boldsymbol{a}_{\text{SRP}}$, $\boldsymbol{a}_{\text{PRP}}$, and $\boldsymbol{a}_{\text{Aero}}$ with a_c. On the other hand, it is also due to the fact that these accelerations are orders of magnitude smaller than the Earth's gravitational acceler-

ations and affect the dynamics to a limited extent. In the frame of linear perturbation theory [28], this allows to linearly correlate the magnitude of the SRP, PRP, and aerodynamic accelerations with Δh, thus resulting in the linear behaviour observed in Fig. 9. This result allows to infer the orbit-raising performance of solar sails for values of a_c between $a_c^{ref}/10$ and $10a_c^{ref}$. This range of characteristic accelerations is representative of a wide spectrum of sailcraft performance, from very limited to futuristic performance. Therefore, interpolation of the results presented in Fig. 9 can be conducted to forecast the orbit-raising capabilities of a broad variety of sailcraft, hence proving valuable for the preliminary design of future solar-sail missions.

Similar to Fig. 9, Fig. 10 gives the results for the inclination-changing case, displaying the achievable inclination gains, Δi, for the three characteristic accelerations considered. Unlike the the orbit-raising case, the way in which Δi varies with the orbital altitude and LTAN strongly depends on the characteristic acceleration, a_c. As can be seen, the minimum altitude for which the sailcraft can manoeuvre without deorbiting changes considerably between the three cases, ranging from 350 km for $a_c = a_c^{ref}/10$ to 600 km for $a_c = 10a_c^{ref}$. This is due to the stronger aerodynamic forces acting on the sailcraft for lower a_c values, which enhance the deorbiting effect. Figure 10 also shows that, for $a_c < a_c^{ref}$, the LTANs corresponding to the best manoeuvring performance lie at around 12:00 (noon-midnight orbits). This is in contrast to the results found for $a_c \geq a_c^{ref}$. Indeed, in these cases the largest inclination gains are obtained for LTANs at around 06:00 or 18:00 (dawn-dusk orbits), as highlighted by the vertical bands of the contour plots. Also, for these loading parameters and within these bands, the Δi gains scale approximately in a proportional way with a_c. Similar to the orbit-raising case, this result is due to the small magnitude of the sailcraft accelerations, which allows to linearly correlate the characteristic acceleration with Δi.

5. Conclusions

This paper presents a trajectory optimisation method to increase the altitude and inclination of sailcraft in a locally optimal manner while accounting for high-fidelity solar-sail dynamics. This optimisation algorithm is based on a grid-search approach used to discretise the set of all possible sailcraft accelerations at any given time. In order to tune the optimiser, a first-order analysis of the achievable accelerations in proximity of the Earth has been performed, showing that the most dynamically complex region around the Earth is found in proximity of the subsolar point for altitudes in the range $[550, 950]$ km. The trajectory optimiser has been used to perform different large-scale parametric analyses, so as to fully characterise the manoeuvring capabilities of Earth-bound sailcraft. To this aim, a wide range of orbits, solar activities, and sailcraft characteristics has been considered, using NASA's recently launched ACS3 solar sail as baseline. The results show that accounting for the planetary radiation pressure acceleration in the sailcraft control proves beneficial to the manoeuvring capabilities of Earth-bound solar sails. Indeed, exploiting planetary radiation allows for 10% to 20% larger gains in altitude and inclination especially for noon-midnight orbits, as the sailcraft passes close to the subsolar point where albedo radiation is particularly strong. The analyses also highlighted that solar sails can perform in-plane and out-of-plane manoeuvres most efficiently for dawn-dusk orbits, as the sailcraft avoids the eclipse region. The presence of atmospheric drag was found to strongly limit the sailcraft manoeuvrability at low altitudes, rendering orbit raising and inclination changing not feasible for altitudes below $450 - 600$ km and $400 - 500$ km, respectively, depending on the intensity of solar activity. Finally, the analyses also showed that the achievable altitude gain scales linearly with the solar-sail characteristic acceleration, while the achievable inclination increase does so only for large-enough characteristic accelerations.

Acknowledgements

The authors express their gratitude to W. Keats Wilkie from NASA Langley Research Center and the entire ACS3 mission team for the insightful discussions on the mission and valuable information shared.

References

[1] C. R. McInnes, *Solar Sailing: Technology, Dynamics and Mission Applications*. Springer Science & Business Media, 2004.

[2] P. Zhao, C. Wu, and Y. Li, "Design and Application of Solar Sailing: A Review on Key Technologies," *Chinese Journal of Aeronautics*, vol. 36, no. 5, pp. 125–144, 2023. DOI: https://doi.org/10.1016/j.cja.2022.11.002.

[3] D. A. Spencer, L. Johnson, and A. C. Long, "Solar Sailing Technology Challenges," *Aerospace Science and Technology*, vol. 93, p. 105 276, 2019. DOI: https://doi.org/10.1016/j.ast.2019.07.009.

[4] M. Macdonald and C. MInnes, "Solar Sail Science Mission Applications and Advancement," *Advances in Space Research*, vol. 48, no. 11, pp. 1702–1716, 2011. DOI: https://doi.org/10.1016/j.asr.2011.03.018.

[5] W. K. Wilkie, "Overview of the NASA Advanced Composite Solar Sail System (ACS3) Technology Demonstration Project," in *AIAA Scitech 2021 Forum*, 2021, p. 1260.

[6] M. Macdonald, *Advances in Solar Sailing*. Springer Science & Business Media, 2014.

[7] L. Carzana, P. Visser, and J. Heiligers, "A New Model for the Planetary Radiation Pressure Acceleration for Solar Sails," *Journal of Guidance, Control, and Dynamics*, pp. 1–14, 2024. DOI: https://doi.org/10.2514/1.G007668.

[8] N. Miguel and C. Colombo, "Deorbiting Spacecraft with Passively Stabilised Attitude using a Simplified Quasi-rhombic-pyramid Sail," *Advances in Space Research*, vol. 67, no. 9, pp. 2561–2576, 2021, Solar Sailing: Concepts, Technology, and Missions II. DOI: https://doi.org/10.1016/j.asr.2020.03.028.

[9] N. Miguel, C. Colombo, *et al.*, "Planar Orbit and Attitude Dynamics of an Earth-orbiting Solar Sail under J2 and Atmospheric Drag Effects," *Advances in the Astronautical Sciences*, vol. 167, pp. 299–319, 2018.

[10] C. Colombo, A. Rossi, F. Vedova, V. Braun, B. Bastida Virgili, H. Krag, *et al.*, "Drag and Solar Sail Deorbiting: Re-entry Time versus Cumulative Collision Probability," in *International Astronautical Congress: IAC Proceedings*, International Astronautical Federation, IAF, 2017, pp. 3535–3553.

[11] A. Ionel, "Deorbiting Upper-stages in LEO at EOM using Solar Sails," *INCAS Bull*, vol. 9, no. 2, pp. 117–132, 2017.

[12] P. C. Roberts and P. G. Harkness, "Drag Sail for End-of-life Disposal from Low Earth Orbit," *Journal of Spacecraft and Rockets*, vol. 44, no. 6, pp. 1195–1203, 2007.

[13] V. Stolbunov, M. Ceriotti, C. Colombo, and C. R. McInnes, "Optimal Law for Inclination Change in an Atmosphere Through Solar Sailing," *Journal of Guidance, Control, and Dynamics*, vol. 36, no. 5, pp. 1310–1323, 2013. DOI: https://doi.org/10.2514/1.59931.

[14] G. Mengali and A. A. Quarta, "Near-optimal Solar-sail Orbit-raising from Low Earth Orbit," *Journal of Spacecraft and Rockets*, vol. 42, no. 5, pp. 954–958, 2005. DOI: https://doi.org/10.2514/1.14184.

[15] T. Morgan, "The Inclination Change for Solar Sails and Low Earth Orbit," *Advances in Astronautical Sciences*, pp. 559–573, 1979.

[16] L. Carzana, P. Visser, and J. Heiligers, "Locally Optimal Control Laws for Earth-bound Solar Sailing with Atmospheric Drag," *Aerospace Science and Technology*, vol. 127, p. 107 666, 2022. DOI: https://doi.org/10.1016/j.ast.2022.107666.

[17] L. Carzana, P. Visser, and J. Heiligers, "A New Model for the Planetary Radiation Pressure Acceleration for Optical Solar Sails," in *6th International Symposium on Space Sailing*, 2023. [Online]. Available: https://www.citytech.cuny.edu/isss2023/docs/isss2023_proceedings.pdf.

[18] A. De Iuliis, F. Ciampa, L. Felicetti, and M. Ceriotti, "Sailing with Solar and Planetary Radiation Pressure," *Advances in Space Research*, vol. 67, no. 9, pp. 2795–2811, 2021. DOI: https://doi.org/10.1016/j.asr.2019.11.036.

[19] A. Barles, M. Ceriotti, F. Ciampa, and L. Felicetti, "An Optimal Steering Law for Sailing with Solar and Planetary Radiation Pressure," *Aerospace Science and Technology*, vol. 118, p. 107 051, 2021. DOI: https://doi.org/10.1016/j.ast.2021.107051.

[20] J. R. Wertz, W. J. Larson, D. Kirkpatrick, and D. Klungle, *Space Mission Analysis and Design*. Springer, 2005.

[21] N. K. Pavlis, S. A. Holmes, S. C. Kenyon, and J. K. Factor, "The Development and Evaluation of the Earth Gravitational Model 2008 (EGM2008)," *Journal of geophysical research: solid earth*, vol. 117, no. B4, 2012.

[22] K. Yeo, N. Krivova, and S. Solanki, "Solar Cycle Variation in Solar Irradiance," *Space Science Reviews*, vol. 186, pp. 137–167, 2014.

[23] E. Tiesinga, P. J. Mohr, D. B. Newell, and B. N. Taylor, "CODATA Recommended Values of the Fundamental Physical Constants: 2018," *Journal of physical and chemical reference data*, vol. 50, no. 3, 2021.

[24] O. Montenbruck and E. Gill, *Satellite Orbits: Models, Methods and Applications*, 1st. Berlin, Germany: Springer-Verlag, 2000.

[25] J. Storch, "Aerodynamic Disturbances on Spacecraft in Free-molecular Flow," *Aerospace Corporation EL Segundo CA Vehicle Systems DIV*, 2002.

[26] J. M. Picone, A. E. Hedin, D. P. Drob, and A. C. Aikin, "NRLMSISE-00 Empirical Model of the Atmosphere: Statistical Comparisons and Scientific Issues," *Journal of Geophysical Research: Space Physics*, vol. 107, no. A12, SIA 15-1-SIA 15–16, 2002. DOI: https://doi.org/10.1029/2002JA009430.

[27] NASA Marshall Space Flight Center. "Marshall Solar Cycle Forecast of August 2024." accessed on 20 September 2024. (), [Online]. Available: https://www.nasa.gov/solar-cycle-progression-and-forecast/archived-forecast/.

[28] V. R. Bond and M. C. Allman, *Modern Astrodynamics: Fundamentals and Perturbation Methods*. Princeton University Press, 1996, vol. 51.